On the influence of eccentricity on Thick Adherend Shear Tests

J.-B. Charpentier, C. Perderiset, Jean-Luc Bouvard, Frédéric Georgi, D. Pino-Muñoz, F. Rasselet

Version of Record: https://www.sciencedirect.com/science/article/pii/S0143749621001081
Manuscript_08feccb1d4eec18ab033b0e3802ef859

On the influence of eccentricity on Thick Adherend Shear Tests

J.-B. Charpentier[a,*], C. Perderiset[a,b], J. L. Bouvard[a], F. Georgi[a], D. Pino-Muñoz[a] and F. Rasselet[b]

[a]*MINES ParisTech, PSL Research University-CEMEF, Centre de Mise en Forme des Matériaux, CNRS UMR 7635, Sophia-Antipolis, France*
[b]*Safran Aircraft Engines, Rond-point René Ravaud, 77550 Moissy-Cramayel, France*

ARTICLE INFO

Keywords:
Finite Element Analysis
Thick Adherend Shear Test
Cohesive Zone
Mode-mixity

ABSTRACT

Two main mechanical tests are commonly used to measure the critical shear stress of an adhesive, the Single Lap Shear (SLS) test and the Thick Adherend Shear Test (TAST). In these tests, the assessment is performed with mode mixity. In this work, a two-dimensional Finite Element Model of an asymmetric TAST is set-up and a few mechanical tests are performed on titanium/epoxy specimens. The model takes into account a shift of the adhesive joint on the loading axis. The impact of a shifted loading is estimated on two specimen geometries though a sensitivity analysis. Then, a method is suggested to assess the state of stress that caused the specimen failure. The results show that the failure location and the mode mixity can be tuned by the shift. Furthermore, it is shown that a standard TAST geometry is remarkably sensitive to a shifted loading. As a consequence, this parameter should be set with a submillimeter accuracy or modified version of classical shear tests should be used. The reported results are consistent with one another and the method used provides a clear link between the critical stresses of the model and the mechanical response of the specimen until failure.

1. Introduction

Among the set of assembling techniques, adhesive bonding stands as one of the most appealing. This technique presents some remarkable features: it reduces stress concentration, it does not add substantial weight to the overall structure and it may be used to assemble materials of different nature. In the past decades, it spread over various industrial fields including transport (automotives, shipbuilding, aeronautics) and energy (wind turbines, solar panels). The design of structures assembled with adhesive bonding requires a set of mechanical tests allowing to assess the mechanical behavior, strength and fatigue properties of the assembly. The most widespread ones aim at setting the specimen adhesive joint into a uniform state of peeling or shear stress, corresponding to the first and second failure modes. Thus, the experiment outcome may be readily related to the mechanical properties of the adhesive. In shear, the Single Lap Shear (SLS) was the first mechanical test. The main SLS tests used in the literature are the standards ISO 9664 and ASTM 1002. The specimen consists of two thin ($\sim$ 1.6 mm) substrates adhesively bonded by their respective opposite extremities over a substantial length. The specimen is pulled apart at constant speed using a tensile testing machine. The model of Volkersen shows that the shear stress in the joint is not uniform and varies in the vicinity of both substrates extremities. Furthermore, the model of Goland and Reissner [1] shows that the slight eccentricity of the applied load induces a bending moment acting on the lap joint. As a consequence of its flexibility, the overlap rotates and peeling stresses are created at both joint extremities. In order to improve the state of stress in the adhesive joint,

ORCID(S): 0000-0002-3396-3212 (J.-B. Charpentier)

the Thick Adherend Shear Test (TAST) has been developed. The main standards used are ASTM 3165, ISO 11003 and ASTM D5656. The design of a TAST specimen differs in two ways from a SLS one: the substrates are thicker ($\sim 6-9$ mm) and they are bonded along the specimen length and two machined grooves define the sheared zone. Both changes increase the bending stiffness of the specimen. Therefore, the sheared zone rotation and the intensity of peeling stresses in the joint are greatly decreased. Although these changes improved substantially the homogeneity of stresses in the adhesive joint, both limits remain. In addition to the SLS and TAST, the Arcan, scarf, napkin ring tests or modified versions of the TAST were developed to obtain more homogeneous stresses[2, 3]. However, there is no standard corresponding to most of these tests and they require the use of specific or complex geometries compared to the flat sheets used in SLS and TAST.

In shear tests experiments reported with brittle adhesives, failure is often located in the vicinity of the adhesive/adherend interfaces[4–7]. This type of failure is commonly referred to as adhesive or apparent adhesive. Furthermore, the failure locus takes the shape of a "Z" such that the failure happens at both adhesive/adherend interfaces and goes through the bondline[4–7].

In the literature, the physical mechanisms which lead to failure of bonded assemblies are controversial, such that different explanations have been suggested to account for experimental observations[6, 8–14]. In the particular case of shear tests, the strength of the assembly decreases as the bondline width increases. In the early attempts to predict the strength, stresses were analytically or numerically predicted in the mid-plane of the bondline and the failure criterion was based on the maximum stress. Among other predictions, the strength was predicted to increase with the bondline thickness which was inconsistent with the experiments[1]. Subsequent works showed that stresses vary in the bondline thickness such that the maximal stresses are located in the vicinities of the adhesive/adherend interfaces rather than in the mid-plane of the bondline[7, 13, 15, 16]. With the maximal stress criterion, various authors reported a good agreement between their models and experiments. Furthermore, this approach is consistent with the failure locus reported in the literature and with the effects of spew fillets on the strength of the assemblies. Alternatively, the bondline thickness effect has been explained as a consequence of a global yielding of the bondline [11]. However, this is not likely to concern brittle adhesives and leads, in this case, to wide overstimations of assembly strength. Finally, other authors suggested that there is a missing ingredient in common models. For example, Adams and Peppiatt [8] suggested that the lack of explanation for the bondline thickness effect could be a consequence of other factors that are indirectly impacted such as the presence of porosity or micro-cracks. Later, Davies *et al.* [17] tested the validity of this hypothesis. In the light of different types of tests, they concluded that there is no evidence of a substantial effect of the adhesive thickness on its properties. Thus, in shear tests with brittle adhesives, the failure is expected to take place when a stress criterion is fulfilled. In the literature, this criterion is applied to the stress distributions computed within the adhesive bond prior to any crack initiation or propagation.

However, in SLS and TAST without a spew-fillet or substrates beaks, cracks initiation happens at two opposite extremities of the adhesive joint. The specimen failure happens in two steps: cracks progress toward the middle of the overlap until the complete failure occurs[5, 15, 18–20]. As mentioned above, the second step is expected to be controlled by a stress intensity criterion. In contrast, the first shares some common features with the progressive failures observed in Double Cantilever Beam tests. Thus, it is expected to be controlled by an energy criterion. Although there is a set of analytical models which account for different geometries, behaviors, *etc.* [21], their use does not take into account the complex crack propagation which takes place. Cohesive Zone Models (CZMs) provide a consistent framework able to model the failure[22]. Using a numerical method, crack initiation and propagation can be modeled and the stress distribution can be approximated at failure[5, 19, 22, 23]. Furthermore, such models can be used to assess mechanical properties through an inverse identification [24]. However, this procedure does not provide direct information on the stresses that caused the final failure. In particular, the assessment is performed in an unknown mode mixity at failure and thus the physical meaning of the assessed parameters remains unclear. In order to overcome this difficulty, the mode mixity which causes the final failure is investigated with TAST in the present work.

In TAST tests, the displacement is applied through the use of a specific device that allows rotations. This device is responsible for the self-positioning of the specimen parallel to the applied load during the experiment. Tsai *et al.* [25] showed that the use of this device may change the stress uniformity in the adhesive joint mid-plane. In a subsequent work Tsai *et al.* [26] suggested that a numerical modeling of this effect was to assume that the applied load is shifted above or below the adhesive joint mid-plane. Their simulations showed that this shift induces substantial changes of the stresses within the bondline mid-plane. In these mechanical tests, the shift of the applied load, should be set to zero but without a standard procedure the corresponding accuracy can widely vary. Furthermore, in numerous applications where the bondline is loaded in shear the eccentricity of the applied load may vary as well. Hence, in the present work the sensitivity of this test to this eccentricity parameter is estimated. In contrast with previous works, the mode mixity is computed and the sensitivity to this parameter is estimated taking into account the variations of stresses through the bondline thickness.

Thus, the aim of this paper is: (*i*) to evaluate the sensitivity of the assembly to a shifted loading; (*ii*) to assess the stress mixity at failure. This manuscript is organized as follows, the specimens, mechanical tests and the corresponding numerical models are presented in section 2. A sensitivity analysis of the TAST with respect to the load eccentricity is presented in section 3 and finally the mode mixity is assessed in section 4. Finally, practical consequences are presented in section 5.

2. Material and methods

2.1. Experiments

A set of mechanical tests are performed with asymmetric TAST specimens. Two 230×100 mm titanium alloy sheets of respective thickness $t_a = 1.6$ mm and $t_b = 9.5$ mm are glued together with an epoxy resin handled with a nylon knit. This knit remains in the adhesive after the cure. The adhesively bonded face of both sheets are treated with an alkaline solution and then coated with an adhesion promoter. The cure is carried out at a constant temperature of $150°C$ with an applied pressure of 3×10^5 Pa for three hours. The assembly is then machined into specimens of dimensions 100×25 mm with an overlap of 5 mm. For each specimen, the thickness of the joint is measured at 12 positions (6 per side) of the overlap. The average thickness of the adhesive bond is $t_c = 290 \pm 30$ μm (unless otherwise stated). Mechanical tests are performed on a Instron 5567 electromechanical machine at room temperature and at constant speed: $v = 0.5$ mm.min^{-1}. The specimens are held by two identical steel devices such as represented on figure 1. These devices provide two degrees of freedom in rotation to the specimen due to the use of pins. The first is a rotation around the y axis (see figure 1c) and the second is a rotation around the z axis (see figure 1a). The role of these two additional degrees of freedom is to set the specimen parallel to the displacement axes. During the test, an eccentric position of the specimen on the pins imposes a bending moment on the overlap. In the following, the shift D is defined as the distance from the center of the bondline to the axis passing through the middle of the steel devices (see figure 1a). D is an algebraic quantity. It is positive when the shift is on the side of the thicker substrate and negative otherwise (D is positive on figure 1a). The position of the specimen with respect to the axis of the applied displacement is imposed through the use of thin steel sheets installed on the pins (see figure 1a). In this work mechanical tests are performed for $D = 0$ and $D = 2.5$ mm with a bondline thickness of $t_c = 290 \pm 30$ μm and others for $D = -0.4$ and $D = -2.5$ mm with a bondline thickness of $t_c = 200 \pm 17$ μm. Each experiment is reproduced once.

A speckled pattern is applied on one side of the specimens. Each test is recorded with a two-camera image correlation system. Images are centered on the overlap, the spatial size of images is about 40×34 mm with a resolution of 2452×2052 pixels. The time, displacement and force recorded by the Instron machine are synchronized with the imaging system. The frequency of acquisition is constant: $F = 5$ Hz. Images are treated with Vic3D to compute the displacements in the three directions of space. Two rectangular areas (represented in green on figure 2a) are defined at a distance of $L = 12$ mm from both extremities of the overlap. In these areas, the in-plane displacements are decomposed into a rigid body component and a deformation one. In the reported set of experiments, the rigid body motion amplitude is at least three order of magnitudes above the deformation ones. Therefore, the average displacements and rotations at a distance L from the overlap are tracked. Then, a Savitzky-Golay filter is applied to remove the noise from the local displacements measurements. Thus, the overall displacement imposed by the testing machine and a local displacement

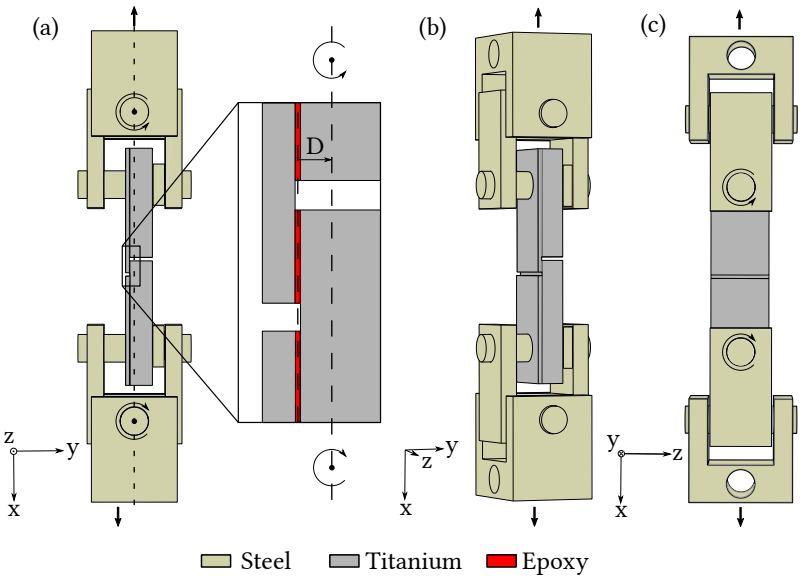

Figure 1: Sketches of a TAST specimen with the holding devices

around the overlap are measured at each acquisition. Finally, after the complete failure of the specimen, the type of failure is attributed according to a visual inspection of the interface. In the reported experiments, only apparent adhesive failures are observed. These results are in agreement with the type of failure reported on epoxy joints with a thickness superior to 100 μm [6, 7].

2.2. Numerical model

The mechanical tests are modeled in $2D$ plane-strain hypothesis. This hypothesis is supported by the important aspect ratio of the bonded joint and the important Young modulus ratio. The model geometry is represented on figure 2. The geometry corresponds to the description made in section 2.1. The overlap of the bonded joint has a thickness of 290 μm (unless otherwise stated). The extremities of the modeled assembly are linked to two rigid bodies and their rotation angles will be referred to as θ_1 and θ_2 respectively. The extremities are set at a distance $L = 12$ mm from the overlap. Its center of rotation is set at a distance 54 mm along the x axis and at an algebraic distance D from the bonded joint mid-plane. As two parts of the specimens and the devices which hold them are not modeled, two springs are added to take into account their compliances. Using the overall and local displacements, the springs compliance is assessed from the linear growth of the force with the displacement at the beginning of the experiments. This method gives a value of $k = 3.75 \times 10^4$ N.mm^{-1}. To model the load, a constant velocity of 0.5 mm.min^{-1} along the x axis is imposed at the outer nodes and there velocities along the y-axis are set to zero.

The titanium substrates are modeled with a linear isotropic elastic material with a Young modulus of 114 GPa and a Poisson coefficient of 0.286. In the following, the adhesive will be modeled either as an elastic or an elasto-

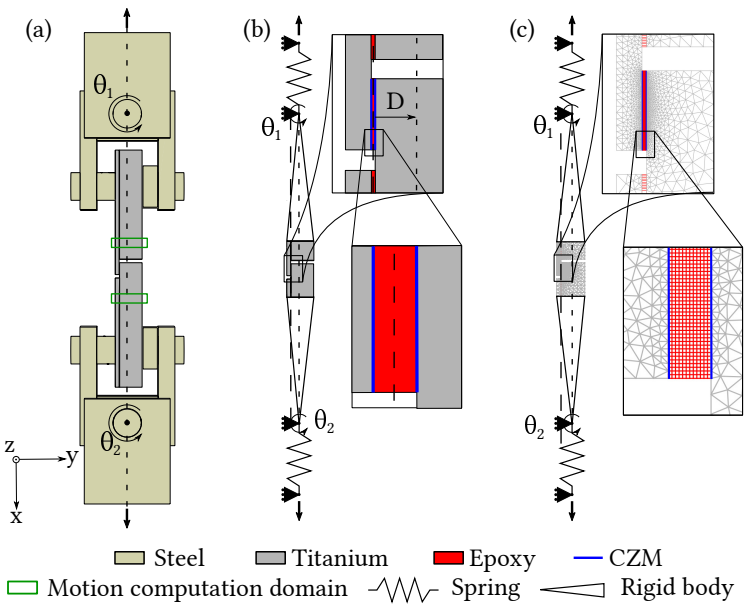

Figure 2: Model of the TAST specimen, from (a) a sketch, to (b) the model, to (c) the meshed geometry

visco-plastic material. In both cases, the elastic response of the adhesive is linear and isotropic, the Young modulus is 1300 MPa and the Poisson coefficient 0.43. In the latter, the yield stress is a function of both the first and the second invariant of the stress tensor. The plasticity is non-associated and relies on a Mahnken-Schlimmer type of model. The model used in the present work has already been described in an other publication [27] and its parameters identified on various mechanical tests on the same epoxy adhesive[28]. The elasto-visco-plastic behavior is detailed in the additional material with the corresponding parameter values. A cohesive zone is introduced at both substrate/adhesive interface of the overlap. The traction-separation relation is bilinear, such as represented on figure 3a. Naming σ_i the stress in mode i and σ_{ic} the corresponding critical stress, the critical stress criterion in a mixed mode loading writes:

$$\left(\frac{\langle\sigma_I\rangle}{\sigma_{Ic}}\right)^2+\left(\frac{\sigma_{II}}{\sigma_{IIc}}\right)^2=1 \tag{1}$$

with I the normal opening mode, II the tangent opening mode and $\langle.\rangle$ the Macauley bracket. Equation 1 is represented on figure 3b. Naming G_i the energy dissipated in the mode i and G_{ic} the total energy dissipated in mode i, the criterion of failure (complete dissipation) in a mixed loading writes:

$$\left(\frac{G_I}{G_{Ic}}\right)+\left(\frac{G_{II}}{G_{IIc}}\right)=1 \tag{2}$$

Note, that the critical parameters σ_{ic} and G_{ic} of equations 1 and 2 are material properties and therefore fixed values. The values of σ_{ic} are *a priori* not known and the values of G_{ic} are in the typical range of toughened epoxy: 250 to 2500 J.m^{-2} [29]. In order to account for the dissipative nature of the cohesive law a damaging variable is introduced such as described in other works [5, 19]. As a consequence loadings and unloadings follow different paths if and only if dissipation occurred during the loading.

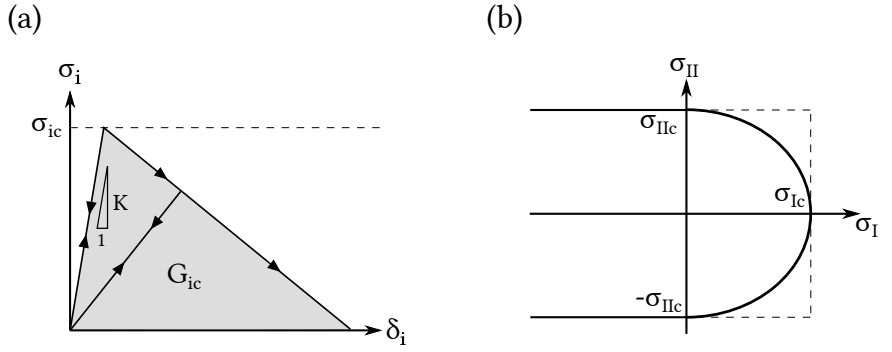

Figure 3: (a) Bilinear traction-seperation relation in mode *i* and (b) Critical stress mixity relation

The model equations are solved numerically with the industrial Finite Element Method (FEM) code Abaqus 6.14. The resolution is implicit and the influence of inertia is neglected in the computation. Unstructured meshes of second order triangular elements are used to solve the mechanical equilibrium in the substrates and structured meshes of first order quadrangular elements are used in the adhesive. First order cohesive elements are used in the cohesive domains. The element size varies from 400 to 40 μm in the substrates and is set to 24 μm in the adhesive. This mesh size was found to be sufficient in the present work (see figure 1 of the additional material). The stiffness K of the bilinear law used is set such that it add a negligible compliance in the system and that it does not induce spurious displacements, $K = 10^6$ MPa.mm^{-1}. Furthermore, the use of a cohesive law may induce some strong convergence difficulties when it is achieved with a Newton-Raphson algorithm. In order to stabilize the convergence, a viscosity has been added to the damaging variable of the cohesive law. The viscosity is chosen such that its characteristic time μ is comparable to the typical time step of the computation $\mu = 10^{-4}$ s. Computations performed for values of μ ranging from 10^{-8} s to 10^{-2} s confirmed that with this value, the viscosity does not impact substantially the results and improves significantly the convergence (see figure 2 of the additional material). Pragmatically, the viscosity is used to ensure that the computation converges when the complete failure arises.

3. Sensitivity to a shifted loading

Prior to any crack initiation, a shifted loading induces a modification of the stresses in the bond line [25, 26]. In this section, an approximation of the stress distribution is built. This approximation describes the main variations of the

shear and peeling stresses in the elastic and elasto-visco-plastic cases. Furthermore, it predicts the existence of intense stresses at specific locations which depend on the shift. Assuming that these intense stesses determine the locus of crack initiation, these predictions are then confronted to experimental observations.

3.1. Modal approximation

The model introduced before predicts stresses within the bondline for a given shift D. Without cohesive zones, it predicts stress distributions prior to any crack initiation. In this case, data reduction can be performed on a given set of stress distributions computed for different shift values. In the present work, the Principal Component Analysis (PCA) is applied to the stress distributions to build a modal decomposition. This decomposition is then used to describe the evolution of stresses as a function of the shift. The same method is employed with the elastic and the elasto-visco-plastic model. It relies on three main steps.

First, $N = 11$ simulations are performed for values of the shift D ranging from -4 to 4 mm. Simulations are stopped at a physical time $t = 60$ s which corresponds to the typical duration of the mechanical tests performed. The shear and peeling (normal to the adhesive/adherent interfaces) stresses, i.e., σ_{xy} and σ_{yy} computed at the end of each simulation, are extracted within each element of the adhesive bond.

Second, the Principal Component Analysis (PCA) is applied to the spatial variations of stresses. To this end, for a given stress type, N vectors $\boldsymbol{\sigma}_i$ of $M = 2400$ components are built from the stress values of a simulation set. Each vector corresponds to the distribution of stresses for a shift value D_i in the bondline. These vectors are set into a $N \times M$ matrix $\boldsymbol{Q}$. The symmetric matrix $\boldsymbol{P} = \boldsymbol{Q}.\boldsymbol{Q}^T$ is then diagonalized. The square roots of the eigenvalues of $\boldsymbol{P}$ are named the λ_j. They are sorted in a decreasing order of magnitude. From the basis of eigenvectors in the N dimensions space, an eigenvector basis is computed in the M dimensions space. In the latter, a vector represents a distribution of shear or peeling stresses in the bondline. Then, the normalized stress eigenvectors $\hat{\boldsymbol{\sigma}}_j$ are used to create an approximation of every $\boldsymbol{\sigma}_i$:

$$\tilde{\boldsymbol{\sigma}}_{k,i} = \sum_{j=1}^{k} c_{i,j} \hat{\boldsymbol{\sigma}}_j \tag{3}$$

with $\tilde{\boldsymbol{\sigma}}_{k,i}$ the k mode(s) approximation of $\boldsymbol{\sigma}_i$ and $c_{i,j}$ the projection of $\boldsymbol{\sigma}_i$ on $\hat{\boldsymbol{\sigma}}_j$. The average error committed in the approximation $\tilde{\boldsymbol{\sigma}}_{k,i}$ of $\boldsymbol{\sigma}_i$ is computed with the metric E_k:

$$E_k = \sqrt{\sum_{i}^{N} (\boldsymbol{\sigma}_i - \tilde{\boldsymbol{\sigma}}_{k,i}).(\boldsymbol{\sigma}_i - \tilde{\boldsymbol{\sigma}}_{k,i})} \Big/ \sqrt{\sum_{i}^{N} \boldsymbol{\sigma}_i.\boldsymbol{\sigma}_i} \tag{4}$$

The eigenvalues λ_k and the error metric E_k are plotted on figure 4 for both models. Regarding the elastic case, it

is noticeable on figure 4a that the use of a two modes approximation corresponds to an error metric of $E_2 \sim 10^{-2}$. Therefore, it provides a reliable stress description. As displayed in figure 4b, the use of an elasto-visco-plastic model for the adhesive leads to an error metric decreasing slowly after the second mode with an associated metric error $E_2 \sim 10^{-1}$ which provides a rough approximation of the stress distributions.

Third, from a mechanical point of view, the specimen location defined by the overlap is subjected to a force and a bending moment. The average angle of rotation $\theta = (\theta_1 - \theta_2)/2$ is an indirect measurement of the bending moment applied to the overlap. For a given adhesive (elastic or elasto-visco-plastic), there is an unique shift D^* such that $\theta = 0$. As the variation of θ is smooth, D^* is computed with a linear interpolation (see figure 3 of the additional material). The corresponding values are $D^* = -0.77$ mm and $D^* = -0.45$ mm in the elastic and elasto-visco-plastic case respectively. The above mentioned two modes approximation relies on a two vector basis $(\hat{\boldsymbol{\sigma}}_1, \hat{\boldsymbol{\sigma}}_2)$. None of these two vectors matches, *a priori*, any remarkable stress distribution. Thus, two new normalized vectors $\hat{\boldsymbol{\sigma}}'_1$ and $\hat{\boldsymbol{\sigma}}'_2$ are computed such that they are normal to each other and that the second corresponds approximately to the stress distribution $\boldsymbol{\sigma}^*$ obtained for $D = D^*$. The corresponding basis $(\hat{\boldsymbol{\sigma}}'_1, \hat{\boldsymbol{\sigma}}'_2)$ generates the same space that the former one. In the following, the stress distributions are projected on this basis and the projections are noted $c'_{i,j}$ instead of $c_{i,j}$. As the other eigenvectors remain unchanged, the projections on these vectors are still noted as $c_{i,j}$.

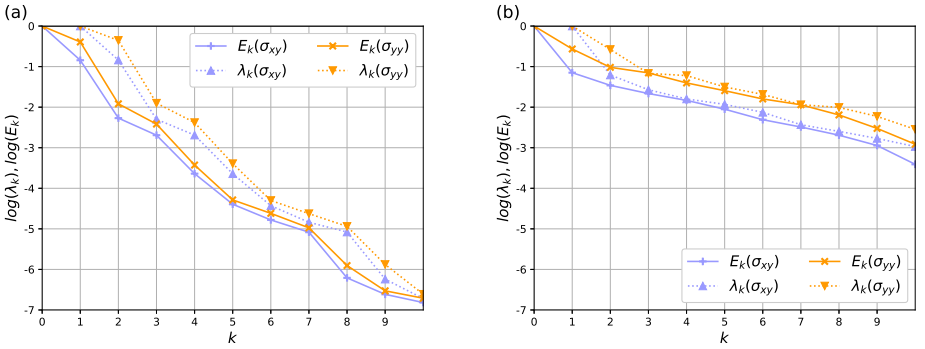

Figure 4: Error metric E_k as a function of the number of modes k used in the approximation and the corresponding eigenvalue λ_k (a) with the elastic model (b) with the elasto-visco-plastic model

3.2. Elastic model

With the elastic adhesive, in shear, the two modes $\hat{\boldsymbol{\sigma}}'_1(\sigma_{xy})$ and $\hat{\boldsymbol{\sigma}}'_2(\sigma_{xy})$ are represented on figure 5b and 5c respectively. The projections of $\boldsymbol{\sigma}_i$ on these two modes (and the third) are represented in cyan in figure 5a as functions of D. The projection on the second mode is greater than the two others in the vicinity of D^*. As a consequence, the shear stress distribution is mainly described by this mode which corresponds to a positive and homogeneous distribution (see figure 5c). In the vicinity of D^*, the projection on the first mode increases slowly and linearly with the shift. Thus, as the shift moves away from D, this mode represents a growing part of the shear stress distribution. There are two main

stress concentrations in this mode (see figure 5b), a positive one near the bottom left corner and a negative one near the top right one. Therefore, when the shift increases from D^*, the shear stress grows rapidly at the bottom left corner. On the contrary, when the shift decreases from D^*, the shear stress grows at the top right corner. Hence, the shift induces the existence of intense shear stresses at one or the other extremities of the bondline. Finally, the projection on the third mode is negligible in the full range of shift values.

The peeling stress modes $\hat{\boldsymbol{\sigma}}'_1(\sigma_{yy})$ and $\hat{\boldsymbol{\sigma}}'_2(\sigma_{yy})$ are represented in figure 5d and 5e respectively. The projections of $\boldsymbol{\sigma}_i$ on these modes are represented in orange in figure 5a. The projection on the first mode increases linearly around D^*. It tends to be the dominant mode for positive shift values. This mode exhibits an intense positive stress concentration at the bottom left corner (see figure 5d). On the contrary, the second mode decreases around D^*. It is the dominant mode for negative shifts. This mode exhibits an intense positive stress concentration at the top right corner (see figure 5e). As a consequence, the main positive peeling stress moves from the top right corner to the bottom left one as D increases. Thus, both the shear and the peeling stresses exhibit the same trend. Once again, the projection on the third mode is negligible on the full range of shift values.

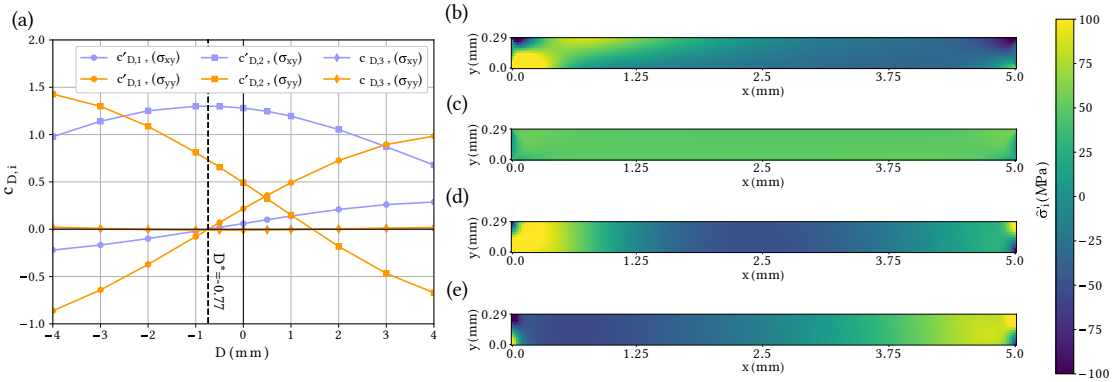

Figure 5: With the elastic model: (a) Projections on the three main eigen modes, where $c'_{D,i}$ is the projection of $\boldsymbol{\sigma}_i$ on $\hat{\boldsymbol{\sigma}}'_i$ and $c'_{D,3}$ the projection of $\boldsymbol{\sigma}_i$ on $\hat{\boldsymbol{\sigma}}_3$ (b) σ_{xy} first mode, (c) σ_{xy} second mode, (d) σ_{yy} first mode, (e) σ_{yy} second mode

3.3. Elasto-visco-plastic model

With the elasto-visco-plastic adhesive, in shear, the two main modes $\hat{\boldsymbol{\sigma}}'_1(\sigma_{xy})$ and $\hat{\boldsymbol{\sigma}}'_2(\sigma_{xy})$ are represented on figure 6b and 6c respectively. The projections of $\boldsymbol{\sigma}_i$ on these two modes (and the third) are represented in cyan in figure 6a as functions of D. In this figure, the projection on the second mode is substantially greater than the two others in the full range of shifts. Thus, the second mode gives a fair idea of the stress distribution. This mode corresponds to a positive and homogeneous stress distribution (see figure 6c). Thus, in contrast with the elastic case, the shear stress remains homogeneous within the bondline even when the shift is important.

The peeling stress modes $\hat{\boldsymbol{\sigma}}'_1(\sigma_{yy})$ and $\hat{\boldsymbol{\sigma}}'_2(\sigma_{yy})$ are represented in figure 6d and 6e respectively. The projections of $\boldsymbol{\sigma}_i$ on these modes are represented in orange in figure 6a. The projections on both modes decrease linearly in the vicinity

of D^* with similar slopes. Both modes correspond to a gradient of peeling stresses with intense stress concentration at the top right and bottom left corners (see figures 6d-e). The strongest negative stress concentration is located in the bottom left corner of the first mode and the strongest positive one is located in the top right corner of the second mode. Therefore, on one side, as D increases, an intense positive peeling stress arises at the bottom left corner. On the other, as D decreases from $D = D^*$, an intense negative peeling stress arises at the top right one. Thus, as concluded in the elastic case, the location of the main stresses goes from the top right corner to the bottom left one when D increases.

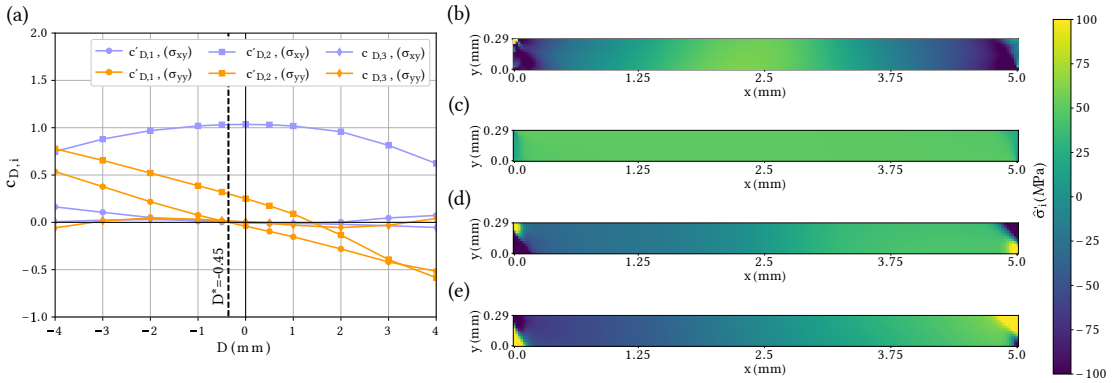

Figure 6: With the elaso-visco-plastic model: (a) Projections on the three main eigen modes, where $c'_{D,i}$ is the projection of $\boldsymbol{\sigma}_i$ on $\hat{\boldsymbol{\sigma}}'_i$ and $c'_{D,3}$ the projection of $\boldsymbol{\sigma}_i$ on $\hat{\boldsymbol{\sigma}}_3$ (b) σ_{xy} first mode, (c) σ_{xy} second mode, (d) σ_{yy} first mode, (e) σ_{yy} second mode

3.4. Types and locus of failure

The elastic and elasto-visco-plastic models predict the existence of intense peeling stress at the top right or the bottom left corners of the adhesive joint. Furthermore, they both predict a transition from the first location to the second as D increases. Assuming that cracking initiates and propagates where the stress concentration is the highest, this analysis predicts that the shift impacts the failure location. The initiation is favored at the top right corner for negative shifts and at the bottom left one for positive ones. These predictions are a consequence of the co-existence of intense peeling stresses at both joint extremities with a rather homogeneous shear stress. Mechanical tests were conducted for D values of -2.5, -0.4, 0 and $+2.5$ mm. Results in term of type of failure are presented in figure 7. All failures have an adhesive appearance but depending on D three conformations are encountered. Two one sided adhesive failures (top or bottom) and a "Z" shaped one. In this later case, crack initiation started from both corners and got through the adhesive joint when the complete failure happened. This result is common for unshifted single lap tests [5, 15, 18–20]. With important shifts, the failures are one sided, no crack initiation or propagation are observed on the opposite interface. The transition of the failure side from the top to the bottom as D increases is thus consistent with the elastic and elasto-visco-plastic analysis. Furthermore, these observations are consistent with the through the thickness variations of stresses within the bondline.

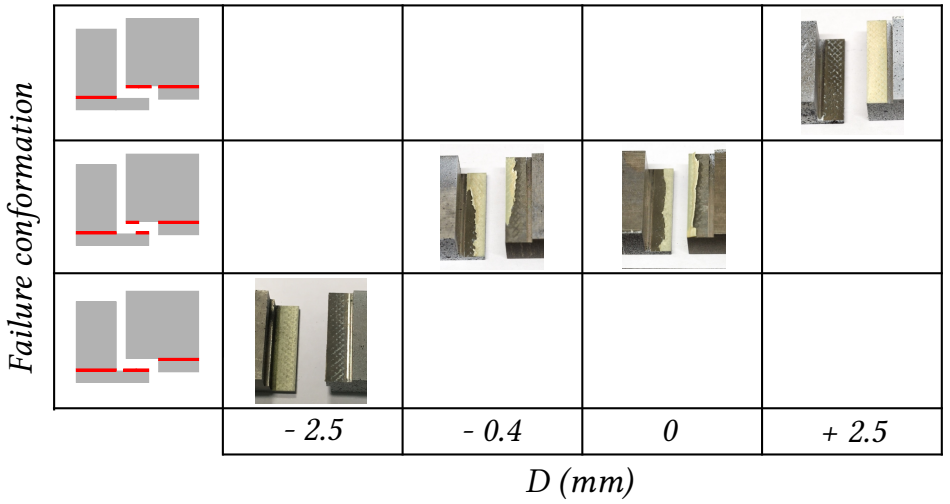

Figure 7: Failure conformation as a function of the shift parameter D

4. Mode mixity at failure

In the last section, it has been shown that the shift influences the spatial distribution of peeling stresses within the bondline which, in turn, influence the failure conformation. This analysis did not take into account the initiation and propagation of cracks prior to the failure. Thus, the state of stress that leads to the failure remains unclear. In this section, the model described in section 2.2 is used to compute the mode mixity at failure. In order to compute its value, the critical stresses are assumed to be unknown and are varied. Then, the critical stresses are assessed from the experimental data to test the consistancy of the method with regard to the experiments. The method employed is based on a meta-model and measures the mode mixity.

4.1. Relation to the mode mixity at failure

In TAST and SLS tests, cracks initiate at the extremities of the adhesive joint[5, 15, 18–20]. Then, cracks propagate toward the middle of the adhesive joint until the final failure which is controlled by the critical stresses. In the numerical model, at failure, the mixed mode critical stress described by equation 1 is reached. Assuming that prior to the failure, the critical stresses have a negligible impact on the stress distribution, therefore, the mode mixity which causes the failure should not depend on the critical stresses. Thus, the equation:

$$\alpha^2 \frac{1}{\sigma_{Ic}^2} + \frac{1}{\sigma_{IIc}^2} = \frac{1}{\sigma_{IIf}^2} \tag{5}$$

describes the condition of failure, with σ_{IIf} the mode II stress at failure and $\alpha = \langle\sigma_{If}\rangle/\sigma_{IIf}$ the mode mixity at failure. As α is assumed constant, the optimal area is expected to be a straight line in a $1/\sigma_{Ic}^2$ vs $1/\sigma_{IIc}^2$ space.

Furthermore, for each simulation, the value of σ_{IIf} corresponds to the shear stress reached at failure. As a consequence, this quantity is expected to be strongly correlated to the maximal force sustained. As a consequence, according to the present description performing multiple simulations with different values of critical stresses should allow the computation of the mode mixity. This method is used in the section below.

4.2. Simulations and mode mixity at failure

The model described in section 2.2 predicts the force as a function of the applied displacement for each pair of critical stresses. In the unshifted case ($D = 0$ mm), 60 simulations are performed. Within this set, σ_{Ic} is picked in the range of 35-65 MPa and σ_{IIc} in the range of 45-65 MPa. For each simulation, the force predicted by the model is compared to the experimental ones using a cost function f_c which grows with the difference between them (see equation 1 of the additional material). Note that the purpose of the cost function is to estimate the variation of the result with a scalar value. In figure 8a, the set of critical stresses pairs is represented along with the cost function. In this figure, the optimal domain takes the shape of a strip of a certain thickness. In the figure 8b, the same set of data is represented in the transformed space ($1/\sigma_{I,c}^2$, $1/\sigma_{II,c}^2$). In this space, the optimal domain takes the shape of a thick straight strip. According to equation 5, the slope of this strip and its position are related to the mode mixity α and the shear stress at failure σ_{IIf}. Using a least square method to compute the slope, this quantity is $\alpha = 0.32$. Using the computed value of α, each simulation corresponds to a value of σ_{IIf} that can be computed troughout equation 5. These values are represented in figure 8c with the maximum force predicted in the corresponding computation. In the figure, all data points collapse on a master curve such that the maximum force is monotonically and positively correlated to σ_{IIf}. Finally, the maximum forces and their corresponding applied displacements are plotted on figure 8d with the experimental curves. In this plot, the points collapse on a thin master curve such that both the force and the applied displacement at failure are strongly correlated to σ_{IIf}. Therefore, this results indicates that the outcome of the model can be predicted by a meta-model based on equation 5 and the master curve. In this figure, the experimental curves are found to exhibit some discrepancy. The value of $sigma_{IIf}$ is computed such that the maximum force predicted with this value is equal to the mean experimental maximum force, $\sigma_{IIf} = 58.7 \pm 7.2$ MPa. The reported uncertainty is directly related to the discrepancy observed on the maximum forces measured.

The same procedure is then applied to the tests performed with the shift $D = +2.5\ mm$. In this case, the critical stress σ_{Ic} is picked in the range of 35-75 MPa and σ_{IIc} in the range of 45-65 MPa. The set of points is represented in the figure 9a with the cost function. Once again, in this space, the optimal domain takes the shape of a strip. In the transformed space, such as represented in figure 9b, it takes the shape of a thick straight strip and its slope is $\alpha = 0.92$. Using this mode-mixity to compute the critical shear stress at failure, this parameter appears to be strongly correlated to the maximum force according to figure 9c. Finally, in figure 9d, the maximum force and the corresponding applied

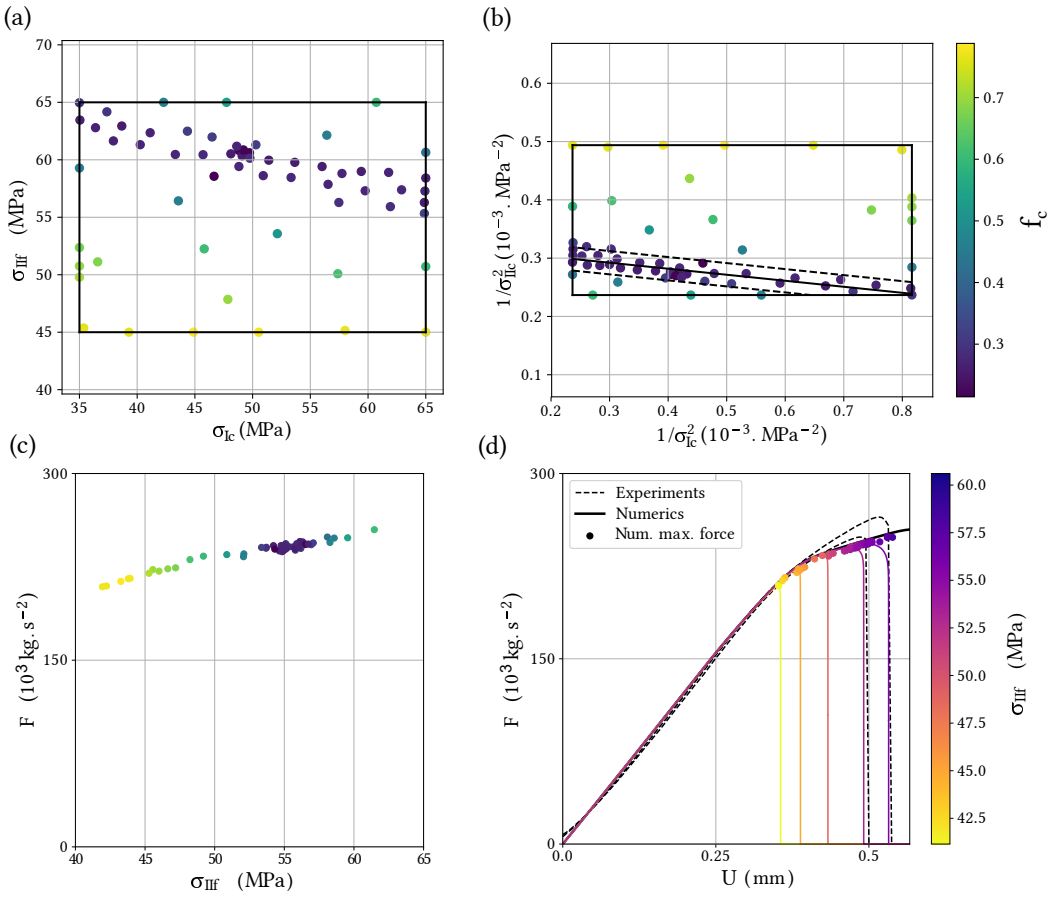

Figure 8: For $D = 0$: (a) Cost function versus σ_{I_c} and σ_{II_c}, (b) Cost function versus $1/\sigma_{I_c}^2$ and $1/\sigma_{II_c}^2$, (c) Numerical maximum force F as a function of σ_{II_f} (d) Experimental force and numerical maximum force vs displacement. The colorbar displayed on figure (b) is shared with (a) and (c).

displacement are found to collapse on a single master curve. Computing σ_{II_c} with the meta-model built upon the master curve and the experimental forces measured, its value is $\sigma_{II_f} = 43.7 \pm 3.4$ MPa.

The same procedure is applied to the tests performed with $D = -0.4$ *mm* and $D = -2.5$ *mm* with a similar success. In this case the bondline was experimentally and numerically thinner, $t_c = 200$ μm. The corresponding master curves are represented on figure 10a-b. The computed mixity and maximum shear stress are $\alpha = 0.47$, $\sigma_{II_f} = 51.8 \pm 1$ MPa and $\alpha = 1.01$, $\sigma_{II_f} = \pm 47.8 \pm 0.8$ MPa respectively. All values of mode mixity are reported in table 1. These values show that the mode mixity increases with the absolute shift. This result is consistant with the analysis presented in section 3.

4.3. Consistency

In the previous section the mode mixity was computed without specified values of critical stresses. Therefore, the results presented might be inconsistant with one another. In this section, the optimal critical stresses are computed

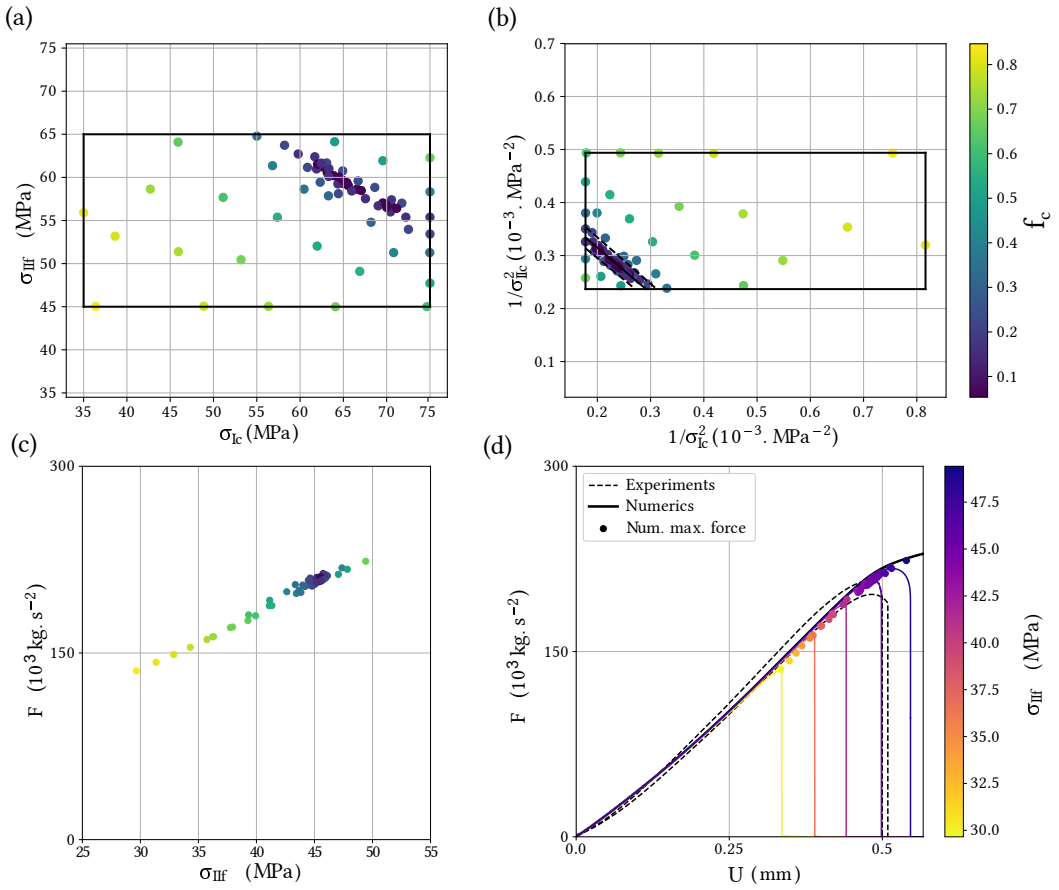

Figure 9: For $D = +2.5\ mm$: (a) Cost function versus σ_{Ic} and σ_{IIc}, (b) Cost function versus $1/\sigma_{Ic}^2$ and $1/\sigma_{IIc}^2$, (c) Numerical maximum force F as a function of σ_{IIf} (d) Experimental force and numerical maximum force vs displacement. The colorbar displayed on figure (b) is shared with (a) and (c).

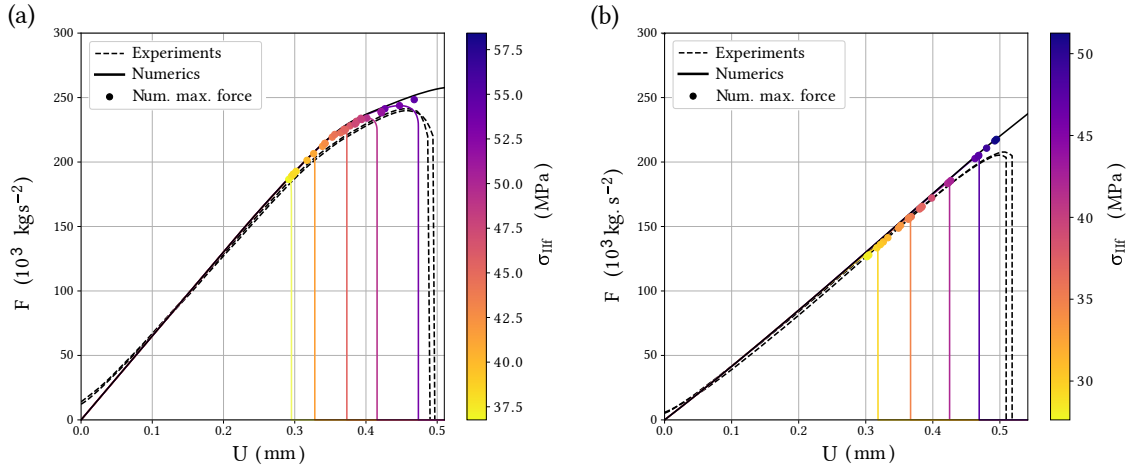

Figure 10: (a) Experimental force and numerical maximum force vs displacement for $D = -0.4$ mm (b) Experimental force and numerical maximum force vs displacement for $D = -2.5$ mm.

with respect to the experimental data. Then, the maximum forces are predicted with the optimal critical stresses and compared to the experimental ones. In the previous section, it has been shown that for each shift value, the maximum force predicted by the model can be accurately predicted by a meta-model based on the mode mixity equation and from the critical stresses. According to the meta-model, the experimental data correspond to specific values of the shear stress at failure with a given uncertainty. According to equation 5, the critical stresses that fulfill the equation at failure are related to each other. The corresponding relations are presented in figure 11a with the associated uncertainty on the shear stress at failure. On this figure, it appears that the curves do not overlap in a single area within their respective uncertainties. The point that appears to be as close as possible to the curves is represented with a black dot. This point corresponds to the black line represented on figure 11b in the stress space. In this figure, the experiments are represented as dots that are positioned above or below the model predictions. The discrepancy appears to be important although the points follow roughly the predictions. Finally, the computed mode-mixity increases with the absolute shift. In figure 11c, the measured force at failure is plotted as a function of the shift. In the figure, the predicted forces are in qualitative agreement with experimental ones. The corresponding values are summarized in table 1.

In the model, mode-mixity plays a key role and influences the force at failure. This is illustrated by the existence of the master curve. In particular, the eccentricity induced by the shift increases the peeling stresses which, in turn, makes the assembly fail at lower forces with different loci of crack initiation (see figures 4-5 of the additional material). These conclusions are consistent with the evolution of the experimental force and crack initiation loci with the shift. Thus, this confirms the relevance of the use of a mixed-mode stress criterion to predict the failure. However, as the mathematical form of this criterion is arbitrary, the computed critical stresses ought to be understood as the parameters that fit the experimental data in the present framework. This is particularly relevant for the first mode critical stress as the mode-mixity does not exceed substantially one.

The TAST specimens used in this work are asymmetric. The results reported in sections 3.2 and 3.3, showed that the optimal loading was slightly shifted. This results is consistent with the intensity of the force predicted in figure 11c, which is maximum for a slightly shifted loading. However, there is no experimental evidence of such an effect. Indeed, in the same figure, the experimental force is maximum for an unshifted loading.

D	−2.5	−0.4	0	2.5	mm
α	1.01	0.47	0.32	0.92	-
F_{exp}	207	241	257	202	10^3 kg.s^{-2}
F_{num}	199	249	246	216	10^3 kg.s^{-2}
$F_{exp} - F_{num}$	8	-8	11	-14	10^3 kg.s^{-2}
σ_{If}	48.5	24.3	18.9	40.3	MPa
σ_{IIf}	47.9	51.8	58.7	43.7	MPa

Table 1
Mode mixity α, experimental and numerical forces F_{exp} and F_{num}, their difference and the stresses at failure. The predicted forces and stresses at failure are given for $\sigma_{Ic} = 74.0$ and $\sigma_{IIc} = 58.7$ MPa.

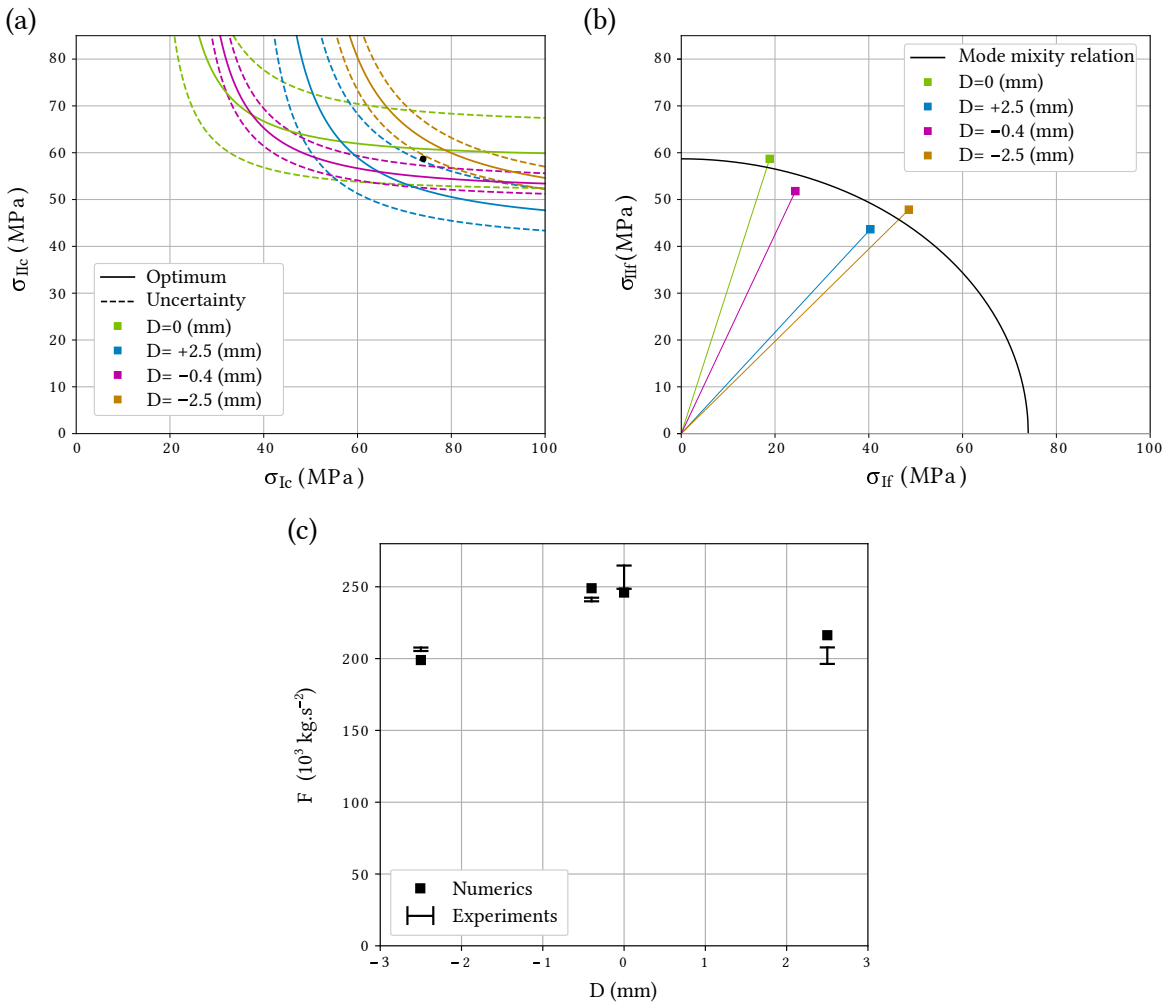

Figure 11: (a) Optimal curves with their respective uncertainties in the parameter space (b) The mode mixity relation with the parameters represented by a dot on figure (a) ($\sigma_{Ic} = 74.0$ and $\sigma_{IIc} = 58.7$ MPa) (c) Maximum experimental and numerical forces (predicted with $\sigma_{Ic} = 74.0$ and $\sigma_{IIc} = 58.7$ MPa)

4.4. Mode-mixity with a TAST standard

In the present work, asymmetric specimens were employed. Thus, the impact of the shift on the mode-mixity is *a priori* different from standard geometries ones. To assess the sensitivity of the standard ISO 11003 to this parameter, the same method has been applied. In this case, the substrates are 6 mm thick, the bondline is kept at $t_c = 290$ μm (unless otherwise stated) and the adhesive is modeled as elastic. The main modes and the corresponding projections are presented on figure 12. The third modes projections ares negligible for all values of D (the error metric and eigenvalues are presented in the figure 6 of the additional material). Hence, the stresses are mainly described by their two main modes. The computed shift without rotation D^* is null. In the figure 12e, intense peeling stresses at the overlap extremities are encountered. As the corresponding projection varies slowly with the shift, their existence is roughly independent of this parameter. In figure 12d, in the vicinity of $D = D^*$ the intensity of the first peeling stress mode is

strongly varying. As this term corresponds to a gradient of peeling stresses, the mode mixity at failure should be quite sensitive to D. This indicates that this TAST standard is sensitive to a shifted loading. To further test the validity of this conclusion, sets of simulations are performed for different critical stresses and different shifts. The method described in section 4.2 is then applied to the results (see figure 7 of the additional material). The computed mode-mixities are reported in figure 13a. The mode-mixity appears to vary strongly with the shift. This observation is consistent with the previous one. The same procedure is applied to unshifted tests with bondlines of different thickness ranging from 290 to 990 μm (see figure 8 of the additional material). The results are reported on figure 13b. The mode mixity appears to double from 290 to 590 μm and is thus quite sensitive to the bondline thickness. Its sensitivity to the bondline thickness is comparable to the one with small shifts. Pragmatically, this implies that the experiments conducted with the standard ISO 11003 should be performed with a controlled shift. For example, the shift could be controlled with a soft piece of matter put around the pins. However, multiple authors presented or used modified versions of classical shear tests [2, 3, 30–32]. The geometry of these tests sets the shift to a given value. In addition, these tests present multiple advantages compared to TAST. Therefore, to perform shear tests we recommand the used of these modified versions instead of classical shear tests.

Finally, the method described in section 4.2 has been applied to different mechanical behaviors, shifts, joint and substrates thicknesses. In each case, the procedure showed the existence of a master curve. This robustness is attributed to the physical mechanism that leads to the failure in the model, i.e., the existence of a criterion based on critical stresses. In the authors' belief, the use of this method presents two main advantages. It gives direct insight into the state of stress that led to the failure in the model through the computed mode-mixity. It provides a meta-model which summarizes the link between the model inputs and outputs. Therefore it is expected to be of relevance in similar works or inverse identifications.

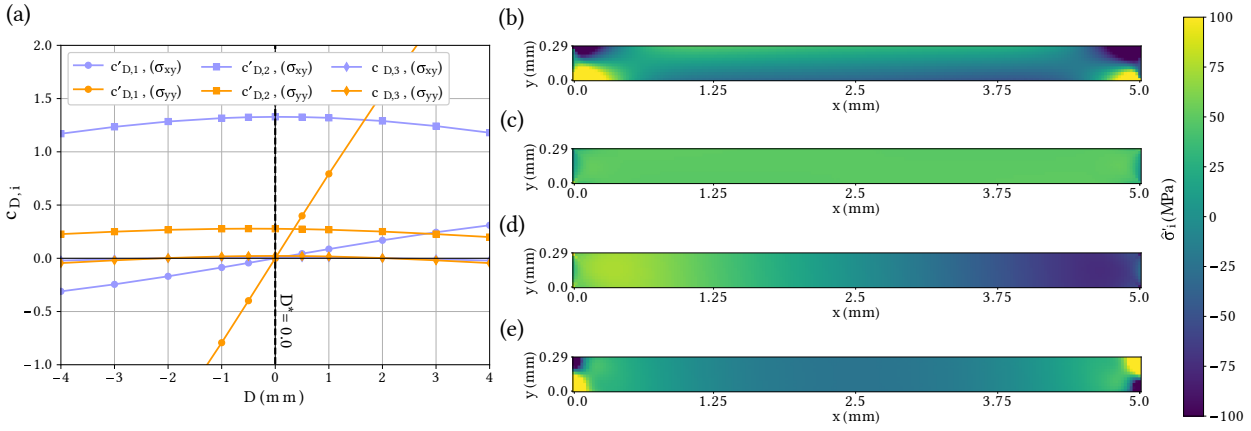

Figure 12: With the elastic model and a geometry such as described in the standard ISO 11003: (a) Projections on the three main eigen modes, where $c'_{D,i}$ is the projection of $\boldsymbol{\sigma}_i$ on $\hat{\boldsymbol{\sigma}}'_i$ and $c'_{D,3}$ the projection of $\boldsymbol{\sigma}_i$ on $\hat{\boldsymbol{\sigma}}_3$ (b) σ_{xy} first mode, (c) σ_{xy} second mode, (d) σ_{yy} first mode, (e) σ_{yy} second mode

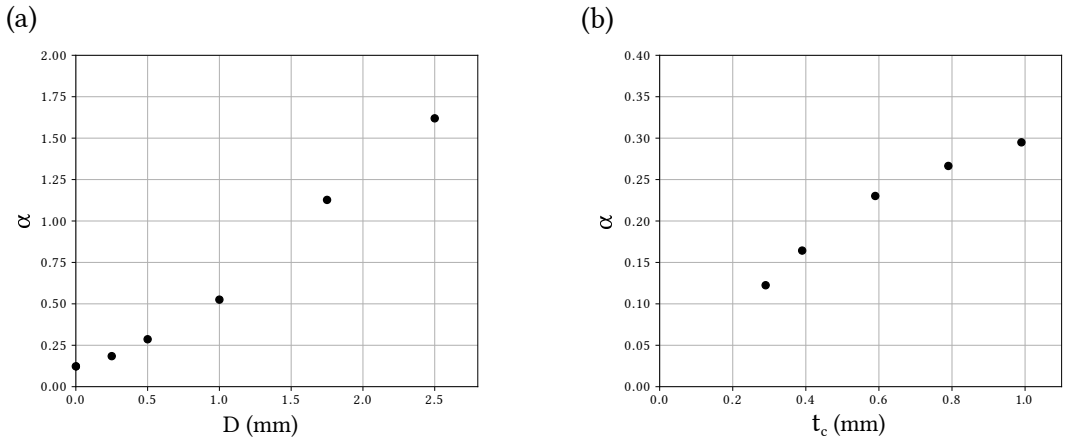

Figure 13: With the elastic model and a geometry such as described in the standard ISO 11003: Mode mixity as a function of (a) the shift parameter D (b) the adhesive bond thickness t_c.

5. Conclusion

In this work, the impact of the mode mixity on a shifted/unshifted loading on the Thick Adherend Shear Test (TAST) has been evaluated. For two different behaviors and geometries, a Principal Component Analysis has been conducted on Finite Element computations. Then, computations were perfomed with cohesive zone elements to assess the mode mixity as a function of the shift. The two main conclusions of the present work are:

(i) The shift changes progressively the crack intiation locus and thus changes the crack conformation.

(ii) A millimetric shift can substantially impact the mode mixity with a standard geometry.

The main practical consequence of (i) is that the crack conformation provides information on the loading that caused the failure. A one sided failure is inconsistant with an unshifted loading. Thus, "Z" shaped failure should be expected and obtained with TAST. The main practical consequence of (ii) is that the holding devices used in TAST standard can create a shift. That shift impacts the mode mixity and therefore can scatter or bias the experimental measurements. In the literature, an increasing number of authors use modified versions of classical shear tests. In these test, the holding devices aren't used and the shift is controlled through the geometry of the specimens. Therefore, we recommand the use of these tests instead of classical ones. Finally, the method presented in section 4 has been applied to various specimen geometries, behaviors and shifts, it is believed to be robust. Among the set of its advantages, it provides a clear link between the model inputs and outputs and thus the sensitivity of the former on the latter. Therefore, this method could be used to investigate other tests or to perform inverse indentifications.

Acknowledgment

The authors wish to express their thankfulness to Sylvain Treutenaere, Matthieu Stackler, William Albouy and Nicolas Carrère from Safran Composite for their advices and help through this study.

References

[1] E. Reissner and M. Goland. The stress in cemented joints. *Journal of Applied Mechanics*, 66:A17–A27, 1944.

[2] J.-Y. Cognard, R. Créac'hcadec, L. Sohier, and D. Leguillon. Influence of adhesive thickness on the behaviour of bonded assemblies under shear loadings using a modified tast fixture. *International Journal of Adhesion and Adhesives*, 30(5):257–266, 2010.

[3] A. Jouan and A. Constantinescu. A critical comparison of shear tests for adhesive joints. *International Journal of Adhesion and Adhesives*, 84:63–79, 2018.

[4] J. Tomblin, C. Yang, and P. Harter. Investigation of thick bondline adhesive joints. Technical report, National Technical Information Service (NTIS), 2001.

[5] J. P. M. Gonçalves, M. F. S. F. De Moura, A. G. Magalhães, and P. M. S. T. De Castro. Application of interface finite elements to three-dimensional progressive failure analysis of adhesive joints. *Fatigue & Fracture of Engineering Materials & Structures*, 26(5):479–486, 2003.

[6] A. A. Taib, R. Boukhili, S. Achiou, S. Gordon, and H. Boukehili. Bonded joints with composite adherends. part i. effect of specimen configuration, adhesive thickness, spew fillet and adherend stiffness on fracture. *International Journal of Adhesion and Adhesives*, 26(4): 226–236, 2006.

[7] L. Da Silva, T. Rodrigues, M. A. V. Figueiredo, M. F. S. F. De Moura, and J. A. G. Chousal. Effect of adhesive type and thickness on the lap shear strength. *The journal of adhesion*, 82(11):1091–1115, 2006.

[8] R. D. Adams and N. A. Peppiatt. Stress analysis of adhesive-bonded lap joints. *Journal of strain analysis*, 9(3):185–196, 1974.

[9] W. D. Bascom and R. L. Cottington. Effect of temperature on the adhesive fracture behavior of an elastomer-epoxy resin. *The Journal of Adhesion*, 7(4):333–346, 1976.

[10] A. J. Kinloch and S. J. Shaw. The fracture resistance of a toughened epoxy adhesive. *The Journal of Adhesion*, 12(1):59–77, 1981.

[11] A. D. Crocombe. Global yielding as a failure criterion for bonded joints. *International Journal of Adhesion and Adhesives*, 9(3):145–153, 1989.

[12] T. Ikeda, A. Yamashita, D. Lee, and N. Miyazaki. Failure of a ductile adhesive layer constrained by hard adherends. *Journal of Engineering Materials and Technology*, 122(1):80–85, 2000.

[13] D. M. Gleich, M. J. L. Van Tooren, and A. Beukers. Analysis and evaluation of bondline thickness effects on failure load in adhesively bonded structures. *Journal of adhesion science and technology*, 15(9):1091–1101, 2001.

[14] L. D. R. Grant, R. D. Adams, and L. da Silva. Experimental and numerical analysis of single-lap joints for the automotive industry. *International journal of adhesion and adhesives*, 29(4):405–413, 2009.

[15] I. U. Ojalvo and H. L. Eidinoff. Bond thickness effects upon stresses in single-lap adhesive joints. *AIAA journal*, 16(3):204–211, 1978.

[16] T. Sawa and H. Uchida. A two-dimensional stress analysis and strength evaluation of band adhesive butt joints subjected to tensile loads. *Journal of adhesion science and technology*, 11(6):811–830, 1997.

[17] P. Davies, L. Sohier, J.-Y. Cognard, A. Bourmaud, D. Choqueuse, E. Rinnert, and R. Créac'hcadec. Influence of adhesive bond line thickness on joint strength. *International journal of adhesion and adhesives*, 29(7):724–736, 2009.

[18] G. D. Dean, B. C. Duncan, R. Adams, R. Thomas, and L. Vaughn. Comparison of bulk and joint specimen tests for determining the shear

properties of adhesives. Technical report, 1996.

[19] R. D. S. G. Campilho, M. F. S. F. De Moura, and J. J. M. S. Domingues. Modelling single and double-lap repairs on composite materials. *Composites Science and Technology*, 65(13):1948–1958, 2005.

[20] J. Y. Cognard, R. Créac'hcadec, L. Sohier, and P. Davies. Analysis of the nonlinear behavior of adhesives in bonded assemblies—comparison of tast and arcan tests. *International Journal of Adhesion and Adhesives*, 28(8):393–404, 2008.

[21] L. Da Silva, P. das Neves, R. Adams, and J. K. Spelt. Analytical models of adhesively bonded joints—part i: Literature survey. *International Journal of Adhesion and Adhesives*, 29(3):319–330, 2009.

[22] L. D. C. Ramalho, R. D. S. G. Campilho, J. Belinha, and L. F. M. da Silva. Static strength prediction of adhesive joints: A review. *International Journal of Adhesion and Adhesives*, 96:102451, 2020.

[23] R. D. F. Moreira and R. D. S. G. Campilho. Strength improvement of adhesively-bonded scarf repairs in aluminium structures with external reinforcements. *Engineering Structures*, 101:99–110, 2015.

[24] L. Da Silva and A. Öchsner. *Modeling of adhesively bonded joints*. Springer, 2008.

[25] M. Y. Tsai, J. Morton, R. B. Krieger, and D.W. Oplinger. Experimental investigation of the thick-adherend lap shear test. *Journal of advanced materials*, 27(3):28–36, 1996.

[26] M. Y. Tsai, J. Morton, and D. W. Oplinger. Numerical analysis of a thick-adherend lap shear specimen. *The Journal of Adhesion*, 62(1-4): 257–280, 1997.

[27] J.-Y. Cognard, C. Badulescu, J. Maurice, R. Créac'hcadec, N. Carrère, and P. Védrine. On modelling the behaviour of a ductile adhesive under low temperatures. *International Journal of Adhesion and Adhesives*, 47:46–56, 2013.

[28] J. Destouesse Villa. *Caractérisation et modélisation des joints de colles sous sollicitations bi-axiales statiques*. 2018.

[29] A. Zotti, S. Zuppolini, M. Zarrelli, and A. Borriello. Fracture toughening mechanisms in epoxy adhesives. *Adhesives-Applications and Properties*, 1:257, 2016.

[30] L. Alfonso, C. Badulescu, and N. Carrere. Use of the modified arcan fixture to study the strength of bonded assemblies for automotive applications. *International Journal of Adhesion and Adhesives*, 80:104–114, 2018.

[31] S. Askarinejad, E. Martínez-Pañeda, I. Cuesta, and N. Fleck. Mode ii fracture of an mma adhesive layer: Theory versus experiment. *European Journal of Mechanics-A/Solids*, 86:104133, 2020.

[32] S. Askarinejad, M. D. Thouless, and N. A. Fleck. Failure of a pre-cracked epoxy sandwich layer in shear. *European Journal of Mechanics-A/Solids*, 85:104134, 2021.